# Raman-shifted eye-safe aerosol lidar

Shane D. Mayor and Scott M. Spuler

The design features of, and first observations from, a new elastic backscatter lidar system at a wavelength of 1543 nm are presented. The transmitter utilizes stimulated Raman scattering in high-pressure methane to convert fundamental Nd:YAG radiation by means of the 1st Stokes shift. The wavelength-converting gas cell features multipass operation and internal fans. Unlike previous lidar developments that used Raman scattering in methane, the pump beam is not focused in the present configuration. This feature prevents optical breakdown of the gas inside the cell. Additionally, the gas cell is injection seeded by a diode to improve conversion efficiency and beam quality. The receiver uses a 40.6-cm-diameter telescope and a 200-μm InGaAs avalanche photodiode. The system is capable of operating in a dual-wavelength mode (1064 and 1543 nm simultaneously) for comparison or in a completely eye-safe mode. The system is capable of transmitting an energy of more than 200 mJ/pulse at 10 Hz. Aerosol backscatter data from vertical and horizontal pointing periods are shown. © 2004 Optical Society of America

*OCIS codes:* 010.3640, 280.3640, 140.3550, 280.1100, 280.1120.

## 1. Introduction

Elastic backscatter lidars are useful tools for atmospheric researchers because they are capable of showing the aerosol distribution in the atmosphere in both space and time. Although the backscatter return from these systems is typically uncalibrated, the images that they provide are extremely valuable for identification of boundary layer depth, elevated aerosol layers, wave activity, and sources of pollution. As an example of their usefulness, the National Center for Atmospheric Research (NCAR) Scanning Aerosol Backscatter Lidar (SABL) is one of the instruments most requested by atmospheric investigators despite the fact that it provides only uncalibrated backscatter intensity. Unfortunately the SABL, like many aerosol backscatter lidars, is not eye safe within a certain range of the instrument. This ocular hazard greatly restricts the number of applications and environments in which it can be used. For example, data cannot be collected near airports or in urban areas. Therefore, development of a completely eye-safe aerosol backscatter lidar is a high priority at the NCAR.

There are currently several general approaches to developing an eye-safe lidar. The three broad practical possibilities are (1) operating at wavelengths less than 0.4 μm, (2) using the micropulse technique[1] in the visible part of the spectrum, and (3) operating at wavelengths greater than 1.4 μm. The human eye is particularly vulnerable to wavelengths from 0.4 to 1.4 μm because those wavelengths easily pass through the cornea and the lens and are focused on the retina. Light at wavelengths less than 0.4 μm and greater than 1.4 μm is safely absorbed in the lens and the cornea at energy densities sufficient for lidar applications. Figure 1 shows the maximum eye-safe energy[2] (MEE) for a pulsed laser as a function of wavelength. The MEE is equivalent to the maximum permissible exposure[2] (MPE) multiplied by the beam area. The figure shows that the region from 1.5 to 1.8 μm has the highest permissible energy. With modest beam expansion it is possible to safely transmit more than over 1 J of energy per pulse in this region.

The maximum eye-safe energy remains modestly high for wavelengths longer than 1.8; however, photodetector performance decreases with increasing wavelength. Although Doppler lidars at 2 and 10 μm successfully use a heterodyne detection method, direct-detection lidar in the infrared is best performed at 1.5 μm because of the availability of inexpensive, high-quantum-efficiency detectors that do not require cooling. In addition to these factors,

The authors are with the Atmospheric Technology Division, National Center for Atmospheric Research, P.O. Box 3000, Boulder, Colorado 80307-3000. S. D. Mayor's e-mail address is shane@ucar.edu.

Received 13 October 2003; revised manuscript received 7 March 2004; accepted 7 April 2004.

0003-6935/04/193915-10$15.00/0

© 2004 Optical Society of America

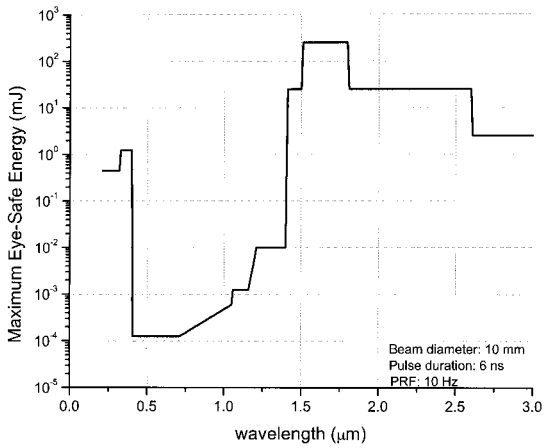


Fig. 1. Maximum eye-safe energy versus wavelength for a 10-mm beam at 10 Hz with a 6-ns pulse duration. PRF, pulse repetition frequency.

work at infrared wavelengths has the advantage compared with the ultraviolet that it features low molecular scattering. Backscattering from molecules is undesirable for aerosol lidars because it reduces the contrast between aerosol backscattering and the noise background. The 1.5-μm wavelength region also features lower sky radiance than a broad range of ultraviolet and visible wavelengths, thus improving the signal-to-noise ratio. Unlike in the visible region, beams in the infrared are invisible and therefore eliminate the possibility of flash blinding pilots or drawing unwanted attention from the public. Finally, working in this wavelength allows one to take advantage of recent advancements in the telecommunications sector (e.g., in detectors, optical coatings, and lasers).

There are a few choices for generating pulsed light in the wavelength region near 1.5 μm. Solid-state methods include optical parametric oscillators[3] (OPOs), solid-state resonators that employ Er:glass or $Cr^{4+}$:YAG,[4,5] and stimulated Raman scattering (SRS). We chose SRS for several reasons, including robustness of technique[6–9] and cost effectiveness. We were especially attracted to the method after a recent publication[10] reported 50% photon conversion efficiency by a method that is resistant to optical breakdown.

## 2. History

Several lidar systems that rely on Raman scattering in $CH_4$ to produce 1.5-μm radiation were created before ours. These designs all focused the pump light in the cell to raise the energy density sufficiently high to cause SRS. A common result of focusing is optical breakdown of the gas, which leads to gradual sooting of the cell windows. The first published results are contained in a paper by Patterson *et al.*;[9] however, the biggest problem reported was that the receiver's field-of-view (FOV) angle was smaller than the divergence of the transmit beam. In the second version of their system, Patterson *et al.* were able to estimate boundary layer height in 15-min intervals by averaging backscatter data over 1000 returns.[11] Carnuth and Trickl[8] presented results of Raman shifting in deuterium and were able to transmit energies of more than 140 mJ/pulse at 10 Hz at 1.560 μm. Spinhirne *et al.*[6] reported on a hard-target-calibrated three-wavelength airborne lidar system at 0.532, 1.064, and 1.540 μm. They used a Raman cell of $CH_4$ also to produce 1.54-μm light and were able to transmit 35 mJ/pulse at 3 Hz. Roy and Mathieu[7] were able to generate 1.5-μm light at 50 Hz by both Raman shifting in methane and use of a solid-state OPO.

In the early 1990s the development of OPOs led to the development of all-solid-state transmitters in several 1.5-μm lidar systems. The all-solid-state approach has the advantage of avoiding the handling of methane and offers more-compact designs. The main disadvantage of OPOs is their large beam divergence at the high power that is necessary for direct-detection lidar.[12] Schwartz Electro-Optics, Inc., developed OPO-type transmitters for use in 1.5-μm lidar systems for NASA and the U.S. Army. The lidar built for NASA is summarized in Phase II SBIR Final Report NAS1-20476,[13] and the report concludes that the system was unable to detect atmospheric aerosol backscatter. The testing of parts of this system was performed at the University of South Florida and was summarized by Harrell[14] and by Harrell *et al.*[15] The work by Schwartz Electro-Optics for the U.S. Army resulted in a helicopter-borne long range biological standoff detection system. This system demonstrated the ability to detect plumes released from crop dusters and surface generators, but its ability to detect naturally occurring aerosols was not documented.[16] Most recently, Richter *et al.*[17] described a solid-state $KTiOAsO_4$–type OPO 1.5-μm lidar system; they transmitted energy of 125-mJ/pulse at 20 Hz at 1.554 μm. Richter *et al.*[17] documented the importance of using custom optics to focus the return on an avalanche photodiode with a 200-μm diameter active area.

The research presented in this paper builds on the research cited above by combining the successful aspects of both, employing a transmitter design that does not focus pump laser light in the Raman cell, and by use of a diode injection seed into the Raman cell to improve the quality of the Stokes beam. The high pulse energy of our pump laser, when it is combined with a reduction in beam diameter, eliminates the need to focus the pump beam in the cell. In this paper we also document the use of custom receiver optics to focus the return onto a 200-μm-diameter photodetector. Such detectors produce 8-dB higher sensitivity than slightly larger (300–500-μm) InGaAs P–I–N detectors.[18] We present time-versus-range images of aerosol backscatter with a temporal resolution of 1 s and a range resolution of approximately 50 m (limited by the bandwidth of our receiver's amplifier). These high-resolution data are of particular value to many meteorologists who wish to image the microscale structure of the atmosphere.

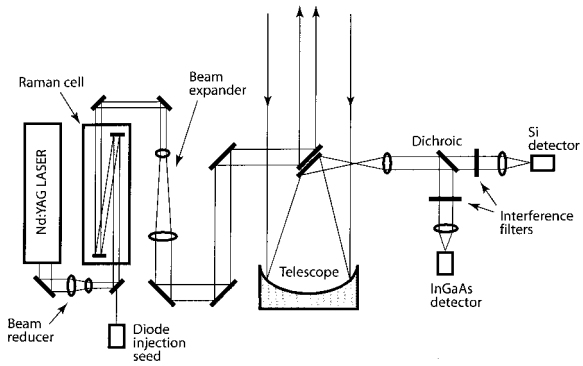


Fig. 2. Schematic of the system with a Newtonian telescope. The data presented in this paper were collected with a Schmidt–Cassegrain telescope, but we plan to use the simpler geometry of the Newtonian in the future.

## 3. Design Goals

In addition to achieving an eye-safe, high-pulse-energy transmitter, we had several other design goals. First, we wished for the transmit beam to be completely within the receiver's FOV beyond a 500-m range. Also, we also wished to use commercially available, high-quantum-efficiency InGaAs avalanche photodiodes (currently the largest available diameter is 200 μm). Mamidipudi and Killinger[19] discussed their difficulty in obtaining a full overlap with biaxial arrangements when they used these small photodetectors. By ray tracing we found that a coaxial transmit–receiver configuration was necessary to achieve full overlap at 500 m with small detectors.

Another important design goal was the ability to transmit and receive at both 1064 and 1543 nm simultaneously for initial testing. There are many lidar systems that operate at 1064 nm because high-power commercial laser sources are easily available at this wavelength and because silicon (Si) avalanche photodiodes (APDs) with relatively large active areas are sensitive and robust for this wavelength. Therefore, although it is not eye safe, we chose to transmit and receive at this wavelength to have a check on the performance of our 1543-nm channel. A diagram of the experimental setup is shown in Fig. 2. We summarize the general specifications for our experimental lidar system in Table 1.

**Table 1. Characteristics of Our Experimental Lidar System**

| Characteristic | Value |
|---|---|
| Transmitter | |
| Wavelength (nm) | 1543 |
| Energy output (mJ) | 220 |
| Pulse repetition frequency (max; Hz) | 10 |
| Divergence (half-angle; mrad) | 0.20 × 0.24 |
| $M^2$ of Nd:YAG pump | 3 × 3 |
| $M^2$ of Stokes beam | 10 × 12 |
| Diameter of transmitted beam (mm) | 50 |
| Pulse duration (ns FWHM) | 4 |
| Receiver | |
| Telescope diameter (cm) | 40 |
| FOV (half-angle; mrad) | 0.27 |
| Filter bandwidth (nm) | 5 |
| Detector | 200-μm InGaAs APD |
| Analog-to-digital sample rate (MHz) | 50 |
| Analog-to-digital resolution (bits) | 14 |

## 4. Transmitter

The full-angle divergence of a laser beam is given by

$$\Theta = M^2 \frac{2\lambda}{\pi w_0}, \tag{1}$$

where $w_0$ is the radius of the beam waist, λ is the wavelength, and $M^2$ is a beam quality factor. $M^2$ is defined as the ratio of the beam's divergence to that of a diffraction-limited beam of the same waist diameter.[20] Note from Eq. (1) that one can reduce the beam divergence by improving the beam quality, increasing the beam diameter (beam expansion), or both. We capitalize on this Gaussian beam propagation concept in our transmitter design to reduce the divergence of the transmit beam to fit within the receiver's field of view. First, the Raman cell is injection seeded to improve beam quality and second, the beam is expanded before it is transmitted into the atmosphere.

For this paper we determined $M^2$ by measuring sets of beam profiles at different $z$ positions in the beam waist range. The beam diameters, calculated by the second-moment method, were combined for the determination of $M^2$ according to International Organization for Standardization standard ISO 11146.

### A. Pump Laser

The transmitter begins with a flash-lamp-pumped, $Q$-switched Nd:YAG laser (Continuum Surelite III) that is capable of generating 800-mJ/pulse energy at 1064-nm wavelength. The laser produces a flat-topped multiple transverse mode beam with pulses of 6-ns FWHM duration. The beam exiting the laser is approximately 9 mm in diameter, with a divergence of 0.6 mrad. Although many pulsed Nd:YAG lasers are commercially available, we chose this model because of its high pulse energy, short pulse length, and relatively low cost.

### B. Stimulated Raman Scattering

The pump beam is converted to the eye-safe wavelength by SRS in a high-pressure cell filled with pure $CH_4$. SRS is a third-order, nonlinear, inelastic scattering process whereby a sufficiently high pump field excites molecular vibrations in a medium. The frequency of the scattered light (Stokes output) is shifted by the frequency of these vibrations. Assuming that the pump is not depleted, the Stokes intensity is given as a function of distance by

$$I_S(z) = I_S(0)\exp(g_R I_p z), \tag{2}$$

in which $I_S(0)$ is the initial Stokes intensity, $g_R$ is the steady-state Raman gain coefficient, $I_p$ is the pump intensity, and $z$ is the interaction length.[21] The gain coefficient is a function of the Raman-active medium and of its pressure. The gain values for methane can be found, along with a thorough overview of SRS, in the literature.[22,23]

The $n$th Stokes, $\lambda_n^{S}$, and anti-Stokes, $\lambda_n^{AS}$, wavelengths are given by

$$\lambda_n^{S} = \left(\frac{1}{\lambda_p} - \frac{n}{\lambda_R}\right)^{-1}, \qquad \lambda_n^{AS} = \left(\frac{1}{\lambda_p} + \frac{n}{\lambda_R}\right)^{-1}, \quad (3)$$

respectively, where $\lambda_p$ is the pump wavelength and $\lambda_R$ is the wavelength of the Raman transition. The wavelength of the Raman-active symmetric stretch of $CH_4$ is 3.428 μm. Pumping with a 1064-nm wavelength results in a 1st Stokes wavelength of 1543 nm, a 2nd Stokes wavelength of 2.808 μm, and a 1st anti-Stokes wavelength of 0.812 μm. As will be noted in the following sections, our Raman cell was designed to suppress the buildup of the 2nd Stokes and 1st anti-Stokes wavelengths.

### C. Injection Seeding

As one can see from Eq. (2), the Stokes intensity is a function of pump intensity, pressure of the gas, interaction path length, and the initial Stokes intensity. Typically the Stokes field is initiated by the spontaneous emission of a photon, and therefore the energy and spatial characteristics will fluctuate. To prevent these fluctuations one can seed the cell with a stable tunable Stokes wavelength laser.[24] We injection seed our Raman cell with a continuous-wave 20-mW telecom diode laser (Mistsubishi FU-68PDF/520M45B). The laser has a center wavelength of 1543.73 nm and approximately 3-nm tunability. It is coupled to a single-mode polarization-maintaining fiber, which emits a nearly perfect Gaussian beam. The laser diode driver and stable temperature controller (Wavelength Electronics Models WLD3343 and WTC3243, respectively) are mounted upon a custom circuit board. The laser can be either current or temperature tuned to match the Stokes emission line. For ease of alignment, the diode output is amplified by a 1-W fiber amplifier (IPG Photonics Corporation Model EAU-1-C) to 100 mW; however, the additional power provides little or no performance enhancement. The output from the laser fiber is expanded and collimated to match the pump beam's diameter, 6 mm, and spatially overlapped by transmission through the back of a gimbal-mounted turning mirror in front of the Raman cell.

### D. Raman Cell

The Raman cell was custom built at NCAR following the design of Kurnit *et al.*[10] but with several mechanical improvements. We used a larger-diameter cylinder (20-cm outside diameter) to accommodate windows in the end caps that provide 25.5-mm clear entrance and exit apertures and 50.8-mm-diameter internal mirrors. The windows are 12.7 mm thick and 38.1 mm in diameter, are made from UV-grade fused silica, and have an antireflection coating for 1.064 and 1.540 μm. The internal mirrors, for multipass operation of the cell, are held by a single independent frame to prevent pressure changes from altering the optical path of the system. The internal mirrors have high-reflectivity coatings at 1064 and 1.540 μm at 0° angle of incidence. They also feature high transmission at the 2nd Stokes line (2.8 μm) and the 1st anti-Stokes line (0.81 μm) to suppress shifting to these wavelengths. The total exterior length of the cell is 75 cm, and the distance between the internal mirrors is 65 cm.

An electrical feed-through in the cell drives an array of eight 24-V dc axial fans inside to circulate the methane. The fans are necessary to clear the gas heated by the preceding laser pulse out of the beam path. Initially, we used a 7.5-cm-diameter tangential wheel fan; however, its performance was compromised by a large motor that ran hot and by bearings that leaked oil. Also, it was difficult to estimate the circulation patterns produced by the tangential wheel fan.

Light is directed into and out of the Raman cell by mirrors in gimbal mounts. The gimbal mounts allow us to adjust the number of times that the beam passes through the cell (three, five, or seven) without adjusting all the other mirrors in the transmit path. Before entering the Raman cell, the pump beam is reduced to 6 mm in diameter by a small Galilean telescope. This increases the energy density in the laser beam for improved frequency conversion. The small Galilean telescope is composed of two 25.4-mm diameter lenses: one plano–convex (CVI part number PLCX-25.4-180.3-UV-1064) and one plano–concave (CVI part number PLCC-25.4-128.8-UV-1064) separated by 12 cm. It is important to note, however, that the pump beam is not focused in the cell. Focusing a high-energy beam in methane often causes optical breakdown and leaves carbon–soot deposits on mirrors and windows—limiting long-term operation of the transmitter.[8,9]

### E. Beam Characteristics

The highest Stokes energy was obtained with a 3.4-m interaction length (five-pass configuration) at pressures from 8.5 to 13.3 atm. In this configuration,

**Table 2. Factors That Influence Range Resolution**

| Characteristic | Frequency | Time (ns) | Equivalent Range Resolution (m) |
|---|---|---|---|
| Pulse duration | | 4 | 1.2 |
| InGaAs APD response (MHz) | 200 | 1.8 | 0.3 |
| Amplifier response (MHz) | 1 | 350 | 53 |
| Digitizer sampling (MSPS) | 100 | | 1.5 |

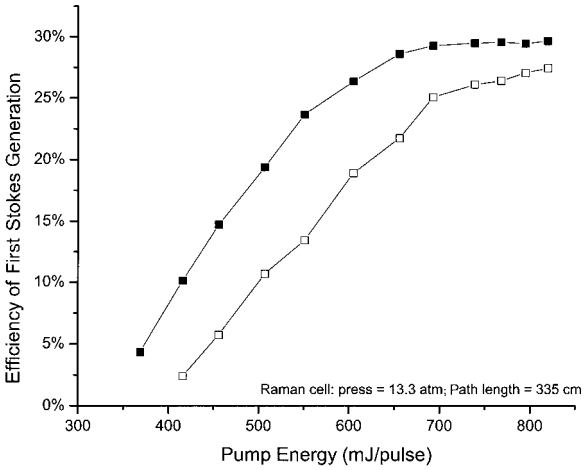


Fig. 3. Input pump energy versus Stokes energy conversion efficiency. The filled and open symbols represent the injection seeder on and off, respectively.

1543-nm energies in excess of 250 mJ/pulse have been obtained with a 800-mJ pump beam, corresponding to better than 30% conversion efficiency. Figure 3 shows pump energy input versus Stokes energy conversion efficiency at a cell pressure of 13.3 atm and at a 3.4-m path length. Figure 4 shows the 1st Stokes energy conversion efficiency as a function of interaction length and cell pressure. A significant enhancement of Stokes conversion efficiency, particularly at lower pressures, is seen with injection seeding. This is noteworthy because we have measured decreased beam quality (higher $M^2$) at higher pressures in the 1st Stokes beam exiting the Raman cell. The conversion efficiency decreased slightly at higher repetition rates, as shown in Fig. 5. This may be an indication that the fans inside the cell do not effectively stir the excited methane molecules out of the beam path. Thermal blooming effects in a high-

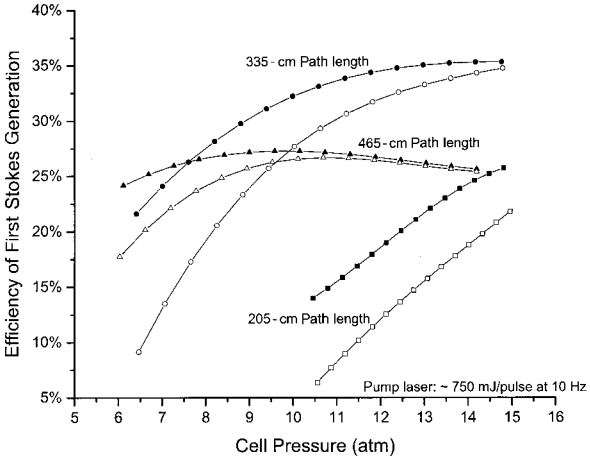


Fig. 4. Stokes energy conversion efficiency versus Raman cell pressure. Three gain lengths are shown, for three-, five-, and seven-pass configurations. Filled and open symbols represent the injection seeder on and off, respectively. The pump energy was 750 mJ in 6 ns.

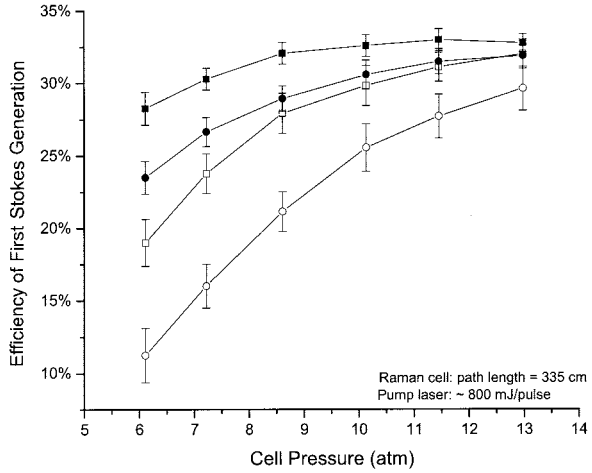


Fig. 5. Stokes energy conversion efficiency versus Raman cell pressure. Two repetition rates are shown: squares, 5 Hz; circles, 10 Hz. The error bars represent the standard deviation of 600 shots. Filled symbols and darker lines, injection seeder on; open symbols and lighter lines, injection seeder off. The pump energy was 800 mJ in 6 ns.

pressure medium are known to limit the conversion efficiency to repetition rates of ≤5 Hz (Ref. 7); however, no degradation in beam quality was measured at the higher repetition rate. The pulse-to-pulse energy fluctuations (standard deviation/mean for 600 shots) are shown as error bars in Fig. 5. Injection seeding reduced the pulse-to-pulse energy fluctuations by approximately 50%. We typically operate the Raman cell at pressures of 8.5–12.0 atm (125–176 psi) and the pump laser at a repetition rate of either 5 or 10 Hz. Under these conditions the 1543-nm beam exiting the Raman cell is 12 mm in diameter, with an $M^2$ of 10 × 12 (the beam was somewhat elliptical), corresponding to a maximum half-angle divergence of 1.0 mrad. The duration of the pulses is approximately 4 ns FWHM.

The linewidth of the Stokes beam, measured with a laser spectrum analyzer with a resolution of 0.9 GHz, was of the order of 40 GHz. Injection seeding did not have any measurable effect on linewidth. If the pump is a single-frequency laser the Stokes linewidth should be approximately 14 GHz at our Raman cell pressures.

### F. Transmitter Operation Modes

The transmitter was designed to work in two modes—a dual-wavelength mode and an eye-safe-only mode. In the dual-wavelength mode the residual pump beam was transmitted simultaneously and coaxially with the eye-safe Stokes beam. This mode was used early in the experiment to permit intercomparison of backscatter from the two wavelengths. In dual-wavelength mode the beams are directed by mirrors coated for high reflectivity at both wavelengths. When the system was operated at the eye-safe wavelength only, we replaced the second gimbaled turning mirror with a custom high-dispersion Pellin–Broca prism. The prism sepa-

rates the residual pump from the eye-safe beam spatially by 1 cm after the beam has propagated 37.5 cm. The prism was designed to operate near the Brewster angle, allowing a transmission of 97% for horizontally polarized light. However, our Nd:YAG laser is ~70% polarized, resulting in a transmission of 90%. This and other losses at turning mirrors reduced the transmit energy of the eye-safe wavelength to roughly 220 mJ/pulse.

### G. Beam Expansion and Transmission Optics

Regardless of whether we are operating in a dual-wavelength or an eye-safe-only mode, we reduce the divergence of the beam(s) before transmission into the atmosphere with a dual-wavelength beam expander in the form of a Galilean telescope. The expander is a custom lens system consisting of two air-spaced doublets, each antireflection coated for 1064 and 1543 nm. The first, 25.4-diameter, doublet is a negative lens with a focal length of 138 mm. The second, 101.6-mm diameter, doublet is a positive lens with a focal length of 574 mm. The doublets are separated by 38 cm and expand the beam 4.3 times. The expanded Stokes beam (50-mm diameter) has a half-angle divergence of 0.20 by 0.24 mrad.

We use a coaxial lidar configuration transmitting off the back of the telescope secondary, and therefore the maximum expanded beam size is limited by the secondary diameter. The expanded transmit beam has the added benefit of reducing the energy density far below the maximum permissible exposure at the 1543-nm wavelength. The expanded beams are directed by gold-coated 101.6-mm-diameter mirrors at a 45° angle of incidence. The edges of the Stokes beam are clipped slightly; for a 99% transmission of a true Gaussian profile beam the mirrors would need to be 5 mm larger. The final mirror, mounted on the back of the telescope secondary, uses electronically controlled Newfocus Picomotors motors to steer the transmit precisely beam to an angle that is within the receiver's FOV.

## 5. Receiver

The receiver's optical layout is shown in Fig. 6. For the results presented here, our prototype lidar system used a commercially available 40.6-cm (16-in.-) diameter $f/10$ Schmidt–Cassegrain telescope (Meade LX200 EMC). The telescope provides a transmission of ~67% at 1.5-μm wavelength. The main loss in transmission is due to the aluminum-coated reflective surfaces, followed by the secondary obscuration, and corrector plate surfaces. In our research we replaced the tertiary mirror with a gold-coated mirror, improving the transmission to ~72%. We intend in the future to use a custom Newtonian telescope (as shown in Fig. 2) with gold-coated mirror surfaces designed to provide ~90% transmission at 1.5 μm.

The telescope is mounted in a fixed vertical position on an optics table. The backscattered light collected by the telescope is collimated with a 25.4-mm-diameter doublet lens to facilitate transmission through subsequent interference filters. The lens is

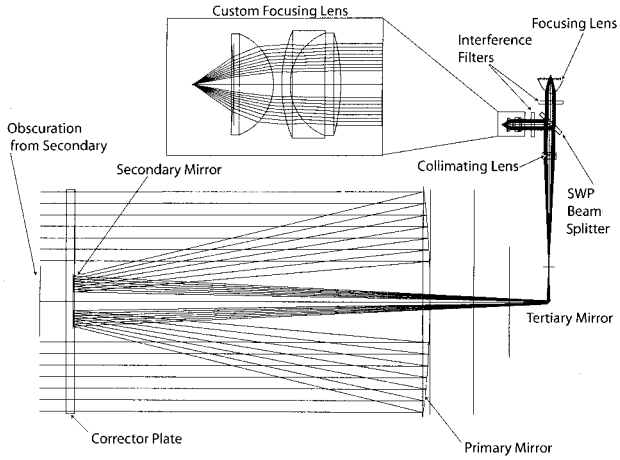


Fig. 6. Ray trace of a receiver using a Schmidt–Cassegrain telescope.

followed by a short-wave-pass (SWP) dichroic beam splitter (CVI, part number SWP-45-1540-1064-PW-2025-C) to separate 1064- and 1543-nm backscatter. The short-wave-pass dichroic mirror has a reflectance of ≥99.5% at 1.540 μm and passes ≥80% at 1064 nm.

The 1064-nm light is filtered by a narrow-bandpass interference filter (Omega Optical, Inc.: 25.4-mm diameter, 1064.2-nm center wavelength, 5-nm FWHM, ≥80% transmission) to reject background light. The light passing through the filter is focused onto a 1.5-mm-diameter active area, long-wavelength enhanced, silicon APD (EG&G Model C30955E) in a LiCEL GbR detector package that includes a low-noise preamplifier. The package includes a single-element aspheric focusing lens and an *XYZ* translation stage.

The eye-safe backscatter return is filtered by a narrow-bandpass interference filter (Omega Optical, Inc.: 25.4-mm diameter, 1543.3-nm center wavelength, 5-nm FWHM, ≥80% transmission). A custom focusing lens was designed to focus the light onto a photodiode. The lens has a three-element design, i.e., a doublet with a companion meniscus lens, with an 18-mm focal length and a 12.4-mm diameter. The lens was designed to collect all light within a 0.15-mrad FOV onto the detector for a range of 500 m–15 km. In practice, the useful range of the instrument, in analogy to the depth of field of a camera is slightly adjustable. For example, by moving the position of the detector with respect to the effective focal plane of the receiver we can shift the full overlap region in either direction. Therefore the results presented in Section 7 below have minimum ranges from 350 to 750 m. The photodetector, in a shielded enclosure, is mounted upon a high-precision three-axis translation stage (Newport ULTRAlign 561D XYZ) for adjustment. The photodetector is a 200-μm-diameter InGaAs/InP APD (EG&G Model C30662) with 75% quantum efficiency, a maximum usable gain of approximately 20, and a bandwidth of 200 MHz.

The half-angle FOV for our receiver system can be given by the photodetector radius divided by the focal length of the receiver system. The effective focal length of the receiver (telescope and custom optics) was calculated to be 367 mm at 1543 nm. Therefore the receiver's FOV, with the 200-μm-diameter detector, is 0.27 mrad (half angle). The receiver's FOV is slightly larger than the transmit beam's divergence of 0.20 by 0.24 mrad. For the 1064-nm channel the effective focal length of the receiver is 446 mm; therefore the receiver's FOV is 1.68 mrad for the 1.5-mm diameter Si APD.

### 6. Data Acquisition

Backscattered photons are converted to electrons by the photodetectors, and the resultant electrical signals are amplified and digitized. For the 1064-nm channel, the LiCEL detector package uses a 10-MHz-bandwidth linear transimpedance amplifier. The 1543-nm signal is amplified by an operational amplifier (Analog Devices Model AD829) that has a bandwidth of 55 MHz at a gain of 20. The optical amplifier, the photodiode, and the power supply are mounted onto a custom circuit board in a rf-shielded case. To amplify return signals that are near the noise level of the detector we operate the operational amplifier with a gain of approximately 850, which unfortunately reduces the bandwidth to approximately 1 MHz (350-ns rise time). We shall discuss the implication of this reduced bandwidth presently.

The analog output of the amplifiers is converted to digital signals by an analog-to-digital card (Gage Model 14100) in a PC. The digitizer card is capable of 14-bit quantization. It is also capable of recording one channel at 100 megasamples per second (MSPS) or two channels at 50 MSPS. Programs are written in Labview to display the backscatter data in real time and to write files to the hard disk. In addition to acquiring backscatter data, the Labview program is capable of simultaneously monitoring laser energies and the temperature and pressure inside the Raman cell by means of serial connections.

Several factors can limit the range-resolving capability of a backscatter lidar system. The first is the laser's pulse length. The 1543-nm pulse duration is 4 ns, which corresponds to 1.2 m in space. Next, the bandwidth (responsiveness) of the photodetector and amplifier must be considered. The InGaAs APD has a bandwidth of 200 MHz with an equivalent rise time of 1.8 ns, which corresponds to approximately 30 cm in range. However, as stated above, the bandwidth of the amplifier described here is 1 MHz, with an equivalent rise time of 350 ns, which corresponds to approximately 53 m in range. Finally, the digitizer's sampling rate controls the spacing of the data points despite the fact that these points may not be independent samples (e.g., if the bandwidth of the detector is significantly slower than the digitizing rate). Our digitizer is capable of processing 100 MSPS in single-channel mode; however, we typically use it in a 50-MSPS dual-channel mode; 50 MSPS is equivalent to 3-m spatial sampling. Therefore, although the data shown have pixels every 3 m in range, the resolution is 53 m. In other words, we currently oversample the backscatter signal. We hope in the future to have a much faster amplifier that can take advantage of the short pulse length and the high-bandwidth photodetector.

### 7. Results

When we collect data with the 1064-nm wavelength from our laboratory we use a vertically pointed 3-cm-wavelength Doppler radar for safety.[25,26] The radar provides a cone of microwave radiation surrounding the transmit beam. Software algorithms that identify aircraft echoes in the radar return turn off the laser immediately if an aircraft is detected.

In the data shown here, we averaged backscatter from consecutive groups of 10 laser shots to form 1-s averages. The backscatter signals were sampled at 50 MHz to provide data points at 3-m intervals in range. The dc baseline of each average return, which is proportional to the background intensity, is subtracted based on an average of data points sampled before the laser is fired. The average lidar return is then corrected for one-over-range-squared dependence. The corrected backscatter intensity data are plotted in Figs. 7 and 8 as time-versus-range color images.

Figure 7 shows backscatter intensity for the 1543- and 1064-nm wavelengths collected simultaneously on 10 July 2003 when the beam was pointed vertically. The time span of the images is 17 min, and the altitude range spans 700 m (from 400 to 1100 m above ground level). Both images in Fig. 7 show the detailed vertical structure of the entrainment zone of a convective boundary layer. A visual comparison of the time-versus height images indicates the 1543-nm data are smoother; we attribute this to the difference in bandwidth of the amplifiers of the two channels. Despite this difference, the comparison shows excellent agreement and demonstrates the ability to resolve fine-scale detail at the eye-safe wavelength of 1543 nm.

To estimate the useful range of the lidar during scanning in a near-horizontal elevation angle, we used a stationary flat turning mirror on the roof of the building to redirect the beam to approximately 3° above the horizon. For these tests we installed the Pellin–Broca prism to separate and prevent the 1064 nm beam from being transmitted. Figure 8 shows backscatter from a 33-min period when the beam was transmitted in the NNE direction with a 3° elevation angle. Consecutive groups of 10 laser shots were averaged to form 1-s averages. The backscatter signal was sampled at 50 MHz to provide 3-m pixels. The figure shows coherent aerosol structures from ~750 m over a 9-km range. We estimate the height of the laser beam to be ~470 m above the surface at 9-km range, neglecting variations in the terrain. The flat turning mirror mount had an aperture of 35.5 cm. Therefore we did not utilize the full collection efficiency of our 40.6-cm telescope and reduced the backscatter signal by 25%. Based on the results of this test, we have demonstrated the feasibility of an eye-safe scanning lidar system. We plan to in-

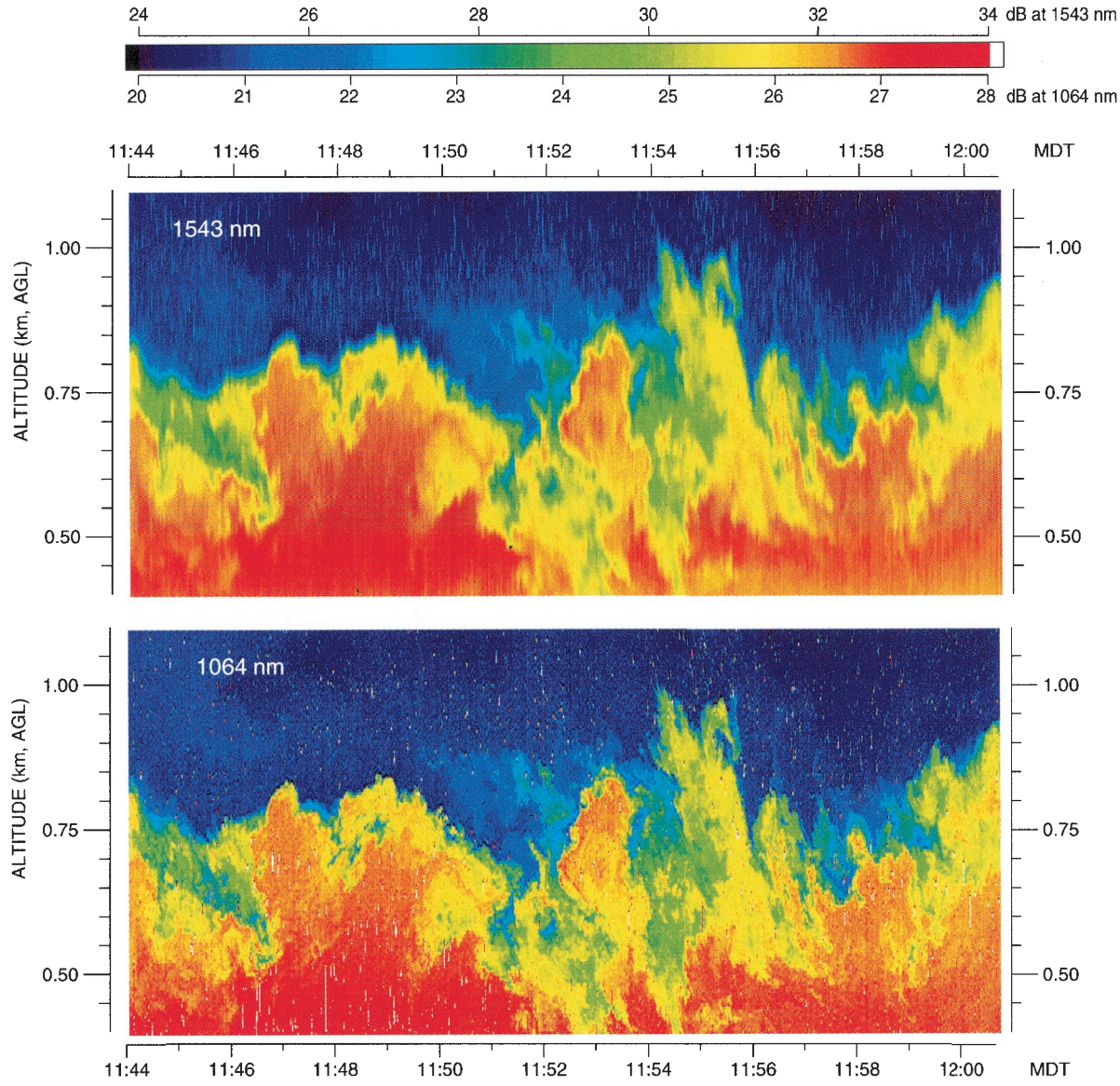


Fig. 7. Time-versus-altitude images of backscatter intensity from the 1543-nm channel and the 1064-nm channel. The data were collected on 10 July 2003 at Boulder, Colorado.

crease the pulse repetition frequency of the pump laser in the future and to obtain a sufficiently large-area beam-steering unit for this purpose.

## 8. Conclusions

In this paper we have described the design of, and preliminary results from, a new uncalibrated aerosol backscatter lidar that operates at the eye-safe wavelength of 1543 nm. The transmitter and receiver capitalize on technologies developed by the telecommunication industry, thereby providing inexpensive, reliable, and off-the-shelf state-of-the-art components. For example, 1550-nm coatings (both antireflection and high-reflection) are often offered on stock optical components.

To test the reliability of the system, we ran the system from our laboratory on 25 days during July and August of 2003. We typically ran the system approximately 6 h per day (for a total of 154 h). The only significant problem experienced was sudden burning of internal gas cell mirrors, which occurred twice. We suspect that the failure was caused by oil droplets released from the internal fan motor or bearings. The problem has not occurred since we replaced the suspect tangential wheel fan with oil-free axial fans. Unlike previous Raman cells used for lidars, the beam geometry used here does not focus the pump light in the cell; therefore it prevents gradual soot buildup on internal cell optics and limits long-term operation. However, the reliability of the Raman cell for continuous use requires further evaluation. For example, we have noticed a slow degradation of the antireflection coating on the interior side of the Raman cell windows. This effect has

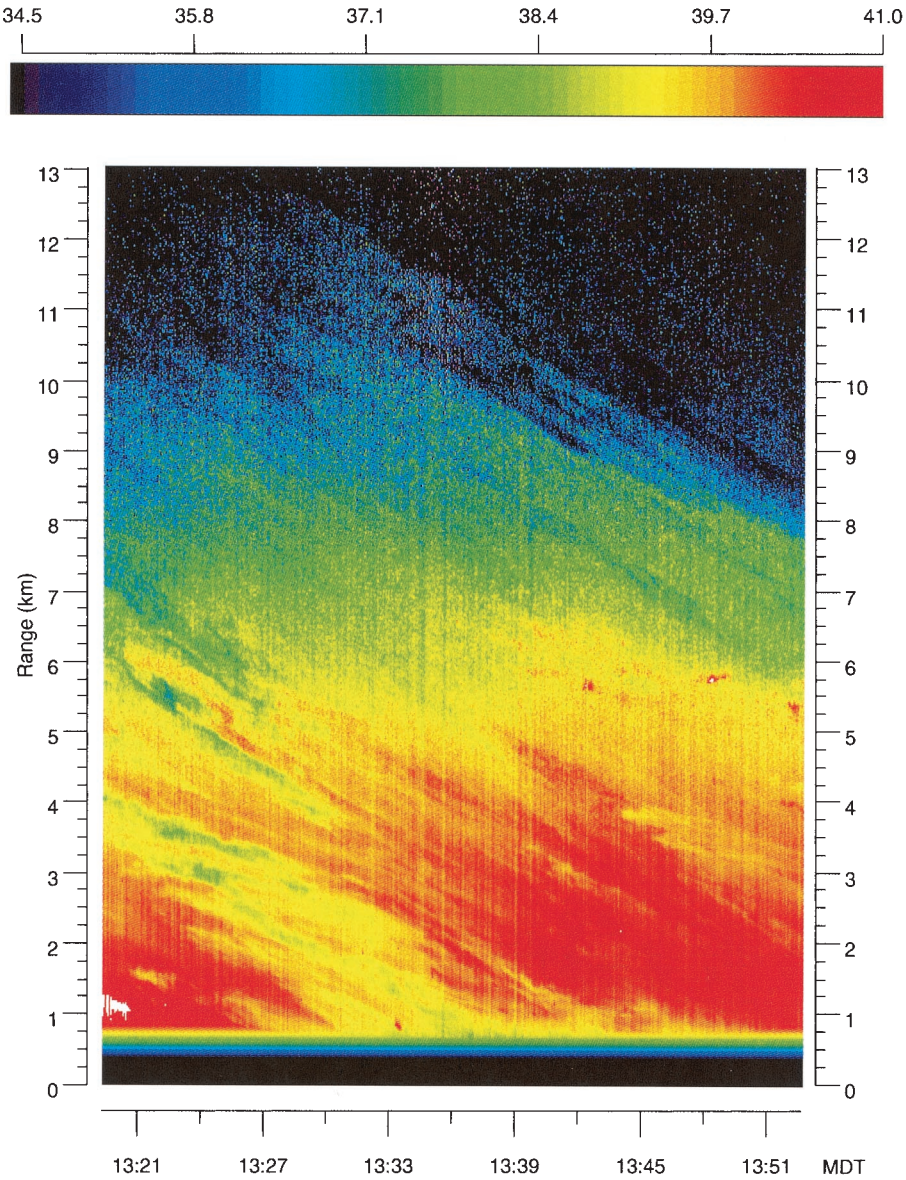


Fig. 8. Time-versus-range images of backscatter intensity from the 1543-nm channel. The data were collected on 18 July 2003 at Boulder, Colorado, while the beam was pointing approximately 3° above the horizon.

been reported in at least one other paper[27] and may be the result of laser-induced photochemical reaction between the $CH_4$ and components of the antireflection coating. We plan to use uncoated windows, oriented at the Brewster angle, in a next-generation Raman cell to prevent this problem. With regard to the reliability of the receiver, we note that we have not experienced any difficulty with maintaining alignment and focus on the detector in our laboratory, which experiences typical cycles in room temperature.

An important achievement was the ability to generate high-energy pulses with good spatial quality. Spatial quality, expressed in terms of $M^2$, is directly related to beam divergence. The receiver's FOV is severely restricted by the relatively small diameter of the detector that we wished to use. Therefore several design features were included to minimize divergence of the transmit beam, maximize the receive FOV, and minimize the range of achieving full overlap. The design features include (1) coaxial transmit beam and receive FOV; (2) injection seeding of Raman cell; (3) transmit beam expander; and (4) custom focusing optics in front of the detector.

Although the time-versus-range data shown depict microscale structures such as aerosol plumes and layers that are of interest to research meteorologists, we are aware that the amplifier for the 1543-nm channel does not have enough bandwidth to respond fully to the bandwidth capability of the InGaAs APD. We plan to develop a second-stage amplifier to overcome this problem and increase the range resolution of the instrument. We also hope to use a higher-power and pulse repetition frequency laser and beam steering

unit for future field applications that require eye-safe scanning.

The development of this instrument was started by S. D. Mayor as part of his NCAR Advanced Studies program postdoctoral fellowship. The majority of the hardware was funded by the 2002 NCAR Director's Opportunity fund, the Advanced Studies program, and the NCAR Atmospheric Technology Division. This research was also supported by the U.S. Department of Energy under the auspices of the Environmental Meteorology Program of the Office of Biological and Environmental Research (grant DE-FG02-04ER63706). We thank Tim Rucker and Eric Lowe for assistance with electrical engineering, Dirk Richter for guidance regarding the diode laser and electronics, Jack Fox for mechanical design of the Raman cell, and Bruce Morley for laboratory work and data-acquisition programming. We appreciate helpful discussions with Ed Eloranta. Norman Kurnit and Bob Karl of Los Alamos National Laboratory graciously shared the details of their Raman cell with us.

## References

1. J. D. Spinhirne, "Micro pulse lidar," IEEE Trans. Geosci. Remote Sens. **31,** 48–55 (1993).
2. American National Standards Institute, "American National Standard for the Safe Use of Lasers, ANSI Z136.1-2000" (American National Standards Institute, New York, 2000), p. 163.
3. M. S. Webb, P. F. Moulton, J. J. Kasinski, R. I. Burnham, G. Loiacono, and R. Stolzenberger, "High-average-power KTiOAsO4 optical parametric oscillator," Opt. Lett. **23,** 1161–1163 (1998).
4. S. Kück, K. Petermann, U. Pohlmann, U. Schönhoff, and G. Huber, "Tunable room-temperature laser action of $Cr^{4+}$-doped $Y_3Sc_xAl_{5-x}O_{12}$," Appl. Phys. B **58,** 153–156 (1994).
5. H. Eilers, W. M. Dennis, W. M. Yen, S. Kück, K. Petermann, G. Huber, and W. Jia, "Performance of a Cr:YAG laser," IEEE J. Quantum Electron. **29,** 2508–2512 (1993).
6. J. D. Spinhirne, S. Chudamani, J. F. Cavanaugh, and J. L. Bufton, "Aerosol and cloud backscatter at 1.06, 1.54, and 0.53 μm by airborne hard-target-calibrated Nd:YAG/methane Raman lidar," Appl. Optics **36,** 3475–3490 (1997).
7. G. Roy and P. Mathieu, "Comparison of Raman and degenerated optical parametric oscillators for a high-energy and high-repetition-rate eye-safe laser," Opt. Eng. **35,** 3579–3584 (1996).
8. W. Carnuth and T. Trickl, "A powerful eyesafe infrared aerosol lidar: application of stimulated Raman backscattering of 1.06 micron radiation," Rev. Sci. Instrum. **65,** 3324–3331 (1994).
9. E. M. Patterson, D. W. Roberts, and G. G. Gimmestad, "Initial measurements using a 1.54-μm eyesafe Raman shifted lidar," Appl. Opt. **28,** 4978–4981 (1989).
10. N. A. Kurnit, R. F. Harrison, R. R. Karl, Jr., J. P. Brucker, J. Busse, W. K. Grace, O. G. Peterson, W. Baird, and W. S. Hungate, "Generation of 1.54 micron radiation with application to an eye-safe laser lidar," in *Proceedings of the International Conference on LASERS '97*, S. Press, ed. (STS, McLean, Va., 1998), pp. 608–610.
11. E. M. Patterson, G. G. Gimmestad, D. W. Roberts, and S. C. Gimmestad, "Boundary layer height measurements with an eyesafe lidar system," in *Optical Remote Sensing of the Atmosphere*, Vol. 5 of 1993 OSA Technical Digest Series (Optical Society of America, Washington, D.C., 1993), pp. 57–60.
12. G. Anstett, A. Borsutzky, and R. Wallenstein, "Investigation of the spatial beam quality of pulsed ns-OPOs," Appl. Phys. B **76,** 541–545 (2003).
13. "High-Energy, Eyesafe Lidar for Long-Range, High-Resolution Aerosol Detection," final report for period from 22 March 1995 to 31 December 1997, contract NAS1-20476 [Phase II, Small Business Innovative Research (SBIR)], prepared for NASA Langley Research Center by Research Division, Schwartz Elecro-Optics, Inc., 135 South Road, Bedford, Mass. 01730.
14. S. R. Harrell, "Atmospheric laser radar measurements using two novel, eye-safe infrared optical parametric oscillators," Ph.D. dissertation (University of South Florida, Tampa, Fla., 1995).
15. S. R. Harrell, W. Wilcox, D. Killinger, G. A. Rines, and R. Schwarz, "High power, eye-safe 1.57 micron OPO lidar for atmospheric boundary layer measurements," in *Optical Instrumentation for Gas Emissions Monitoring and Atmospheric Measurements*, J. Leonelli, D. K. Killinger, W. Vaughan, and M. G. Yost, eds., Proc. SPIE **2366,** 354–357 (1995).
16. I. Acharekar, M., Schwartz Electro-Optics, 3259 Progress Drive, Orlando, Fla. 32826 (personal communication, 2003).
17. D. A. Richter, N. S. Higdon, P. Ponsardin, D. Sanchez, T. H. Chyba, D. A. Temple, W. Gong, R. Battle, M. Edmondson, A. Futrell, D. Harper, L. Haughton, D. Johnson, K. Lewis, and R. S. Payne-Baggott, "Design validation of an eye-safe scanning aerosol lidar with the Center for Lidar and Atmospheric Sciences Students (CLASS) at Hampton University," in *Lidar Remote Sensing for Industry and Environment Monitoring II*, U. N. Singh, ed., Proc. SPIE **4484,** 8–16 (2002).
18. S. G. Hummel, A. Pauchard, M. Bitter, Z. Pan, Y. H. Lo, Y. Kang, P. Mages, and K. L. Yu, "InGaAs-on-Si avalanche photodiodes," IEEE LEOS Newsletter **16,** 3–6 (2002).
19. P. Mamidipudi and D. Killinger, "Optimal detector selection for a 1.5 micron KTP OPO Atmospheric Lidar," in *Laser Radar Technology and Applications IV*, G. W. Kamerman and C. Werner, eds., Proc. SPIE **3707,** 327–335 (1999).
20. T. F. J. Johnston, "$M^2$ concept characterizes beam quality," Laser Focus World 173–183 (May 1990).
21. A. Anderson, *The Raman Effect* (Marcel Dekker, New York, 1971).
22. L. de Schoulepnikoff, V. Mitev, V. Simeonov, B. Calpini, and H. van den Bergh, "Experimental investigation of high-power single pass Raman shifters in the ultraviolet with Nd:YAG and KrF lasers," Appl. Opt. **36,** 5026–5042 (1997).
23. A. Kazzaz, S. Ruschin, I. Shoshan, and G. Ravnitsky, "Stimulated Raman scattering in methane—experimental optimization and numerical model," IEEE J. Quantum Electron. **30,** 3017–3024 (1994).
24. J. G. Wessell, K. Repasky, and L. J. Carlsten, "Efficient seeding of a Raman amplifier with a visible laser diode," Opt. Lett. **19,** 1430–1432 (1994).
25. G. R. Gray and F. Pratte, "An eye-safety radar for lidar operations," in *31st International Conference on Radar Meteorology* (American Meteorological Society, Boston, Mass., 2003), p. P5B.9.
26. F. Pratte, G. R. Gray, and J. Fox, "Airborne proximity radar for laser eye safety: design and development," in *31st International Conference on Radar Meteorology* (American Meteorological Society, Boston, Mass., 2003), p. P5B.10.
27. V. Simeonov, V. Mitev, H. van de Bergh, and B. Calpini, "Raman frequency shifting in a $CH_4$:$H_2$:Ar mixture pumped by the fourth harmonic of a Nd:YAG laser," Appl. Opt. **37,** 7112–7115 (1998).